200031887_LMMP19_04_R1_081204

MATERIALS AND MANUFACTURING PROCESSES
Vol. 19, No. 4, pp. 1–24, 2004

Optimization of Intensities and Orientations of Magnets Controlling Melt Flow During Solidification

George S. Dulikravich,[1,*] Marcelo J. Colaço,[2] Brian H. Dennis,[3] Thomas Martin,[4] Igor N. Egorov-Yegorov,[5] and Seungsoo Lee[6]

[1]Florida International University, Mechanical and Materials Eng. Dept., MAIDROC Lab., Miami, FL, USA
[2]Military Institute of Engineering (IME), Mechanical and Materials Eng. Dept., Rio de Janeiro, Brazil
[3]University of Texas at Arlington, Mechanical and Aerospace Eng. Dept., Arlington, TX, USA
[4]Pratt and Whitney Engine Company, Turbine Discipline Engineering and Optimization Group, East Hartford, CT, USA
[5]Sigma Technology, Moscow, Russia
[6]Inha University, Aerospace Eng. Dept., Incheon, Korea

AQ1

ABSTRACT

When growing large single crystals from a melt, it is desirable to minimize thermally induced convection effects so that solidification is achieved predominantly by thermal conduction. It is expected that under such conditions any impurities that originate from the walls of the crucible will be less likely to migrate into the mushy region and consequently deposit in the crystal. It is also desirable to achieve a distribution of the dopant in the crystal that is as uniform as possible. A finite volume method and a least-squares spectral finite element method were used to develop accurate computer codes for prediction of solidification from a melt

*Correspondence: Prof. George S. Dulikravich, Florida International University, Mechanical and Materials Eng. Dept., MAIDROC Lab., EC 3474, Miami, FL 33027, USA; E-mail: dulikrav@fiu.edu.

DOI: 10.1081/LMMP-200031887
1042-6914 (Print); 1532-2475 (Online)

under the influence of externally applied magnetic fields. A hybrid constrained optimization algorithm and a semi-stochastic self-adapting response surface optimizer were then used with these solidification analysis codes to determine the distributions of the magnets that will minimize the convective flow throughout the melt or in desired regions of the melt only.

AQ2

INTRODUCTION

The objective of this article is to demonstrate the feasibility of determining unknown boundary values of an applied magnetic field that will create user-specified features of the melt flow-field and the melt/solid interface. This article presents a proof-of-concept effort and it does not present the most advanced MHD analysis involving solidification. In this study, all physical properties (density, heat conductivity, heat capacity, electric conductivity, etc.) were treated as constants instead of as functions of temperature. The effects of magnetization were not included. This study does not involve optimization of thermal boundary conditions in MHD solidification.[1]

The latent heat released in the mushy region of a solidifying melt, where $T_{\text{liquidus}} > T > T_{\text{solidus}}$, is assumed to be proportional to the local volumetric liquid/(liquid + solid) ratio.[2,3]

$$f = \frac{V_\ell}{V_\ell + V_s} = \left(\frac{T - T_{\text{solidus}}}{T_{\text{liquidus}} - T_{\text{solidus}}}\right)^n = \tilde{\theta}^n \tag{1}$$

Here, the exponent n is typically $0.2 < n < 5$, while $f = 1$ for $T \geq T_{\text{liquidus}}$ and $f = 0$ for $T \leq T_{\text{solidus}}$. In all test cases, the non-dimensional temperature is given as

$$\theta = \frac{T - T_{\text{solidus}}}{T_h - T_c} \tag{2}$$

Thus, $\theta = 0.0$ corresponds to interface between the solid phase and the mushy region. For relatively small changes of density with temperature, it is justifiable to assume linear variation of density as a function of the temperature.[4] In the liquid, the density is

$$\rho_\ell = \rho_r\left[1 + \left(\frac{\partial(\rho_\ell/\rho_r)}{\partial\theta}\right)_r (\theta - \theta_r)\right] = \rho_r[1 - \alpha_\ell(\theta - \theta_r)] \tag{3}$$

with a similar expression for the solid phase. Therefore, the liquid–solid mixture density and modified heat capacity can be defined as

$$\rho_{\text{mix}} = f\rho_\ell + (1 - f)\rho_s \tag{4}$$

$$c_{\text{mix}} = f\rho_\ell \frac{\partial(c_\ell\theta_\ell)}{\partial\theta} + (1 - f)\rho_s \frac{\partial(c_s^{eq}\theta_s)}{\partial\theta} \tag{5}$$

where an enthalpy method[3] was used to formulate the equivalent specific heat coefficient in the solid phase.

$$c_s^{eq} = c_s - \frac{1}{S_{TE}}\frac{\partial L}{\partial \theta} \tag{6}$$

Here, the specific heat coefficient accounts for the latent heat release in the mushy region. The non-dimensional numbers used in magneto-hydrodynamics (MHD) modeling are as follows:

Reynolds hydrodynamic Prandtl hydrodynamic Eckert number

$$R_e = \frac{\rho_r v_r \ell_r}{\mu_{vr}} \qquad P_R = \frac{\mu_{vr} c_r}{\kappa_r} \qquad E_c = \frac{v_r^2}{c_r \Delta T_r} \tag{7a–c}$$

Grash of number Prandtl magnetic Hartmann number

$$G_R = \frac{\rho_r^2 \alpha_r g_r \Delta T_r \ell_r^3}{\mu_{vr}^2} \qquad P_m = \frac{\mu_{vr}\sigma_r \mu_r}{\rho_r} \qquad H_T = \ell_r \mu_r H_r \left(\frac{\sigma_r}{\mu_{vr}}\right)^{1/2} \tag{7d–f}$$

Stefan number Froude number Rayleigh number

$$S_{TE} = \frac{c_r \Delta T_r}{L_r} \qquad F_R = \frac{v_r^2}{g_r \ell_r} \qquad R_a = \frac{\rho_r^2 \alpha_r c_r g_r \Delta T_r \ell_r^3}{\kappa_r \mu_{vr}} \tag{7g–i}$$

Using these parameters, the non-dimensional formulation of the Navier-Stokes subsystem of the MHD equations for phase-changing mixtures of two liquids has been formulated.[5–7] In this formulation, the solid phase is treated as the second liquid with extremely high viscosity. Assuming that both phases have the same local velocity, the non-dimensional form of mass conservation is obvious.

$$\nabla \cdot \underline{v} = 0 \tag{8}$$

Each phase could have been modeled with its own velocity, which would yield a more complicated expression for multi-component mass conservation.[8] The non-dimensional version of linear momentum conservation for two-phase MHD flows with thermal buoyancy, and magnetic force is

$$\begin{aligned}
&\rho_{\text{mix}} \frac{\partial \underline{v}}{\partial t} + f\rho_\ell \nabla \cdot (\underline{v}\underline{v} + \hat{p}_\ell \underline{\underline{I}}) + (1-f)\rho_s \nabla \cdot (\underline{v}\underline{v} + \hat{p}_s \underline{\underline{I}}) \\
&= f\left\{ \nabla \cdot \left[\frac{\mu_{v\ell}}{R_e} (\nabla \underline{v} + (\nabla \underline{v})^*) \right] + \frac{G_R}{R_e^2} \rho_\ell \alpha_\ell \theta \, \underline{g} + \frac{H_T^2}{P_m R_e^2} \mu_\ell (\nabla \times \underline{H}) \times \underline{H} \right\} \\
&\quad + (1-f)\left\{ \nabla \cdot \left[\frac{\mu_{vs}}{R_e} (\nabla \underline{v} + (\nabla \underline{v})^*) \right] + \frac{G_R}{R_e^2} \rho_s \alpha_s \theta \, \underline{g} + \frac{H_T^2}{P_m R_e^2} \mu_s (\nabla \times \underline{H}) \times \underline{H} \right\}
\end{aligned} \tag{9}$$

where the non-dimensional hydrodynamic, hydrostatic, and magnetic pressures were combined to give

$$\hat{p}_\ell = \frac{p}{\rho_\ell} + \frac{\varphi}{F_R^2} + \frac{H_T^2}{P_m R_e^2} \mu_\ell \underline{H} \cdot \underline{H} \quad \text{and} \quad \hat{p}_s = \frac{p}{\rho_s} + \frac{\varphi}{F_R^2} + \frac{H_T^2}{P_m R_e^2} \mu_s \underline{H} \cdot \underline{H} \tag{10}$$

Here, φ is the non-dimensional gravity potential defined as $\underline{g} = -\nabla\varphi$. Then, the non-dimensional form of energy conservation for incompressible phase-changing MHD flows including Joule heating can be written as[6]

$$c_{\text{mix}}\frac{\partial\theta}{\partial t} + f\rho_\ell\nabla\cdot(c_\ell\theta\underline{v}) + (1-f)\rho_s\nabla\cdot(c_s^{eq}\theta\underline{v})$$

$$= f\left[\frac{1}{R_eP_R}\nabla\cdot(\kappa_\ell\nabla\theta) + \frac{1}{\sigma_\ell}\frac{H_T^2E_c}{P_m^2R_e^3}(\nabla\times\underline{H})\cdot(\nabla\times\underline{H})\right]$$

$$+ (1-f)\left[\frac{1}{R_eP_R}\nabla\cdot(\kappa_s\nabla\theta) + \frac{1}{\sigma_s}\frac{H_T^2E_c}{P_m^2R_e^3}(\nabla\times\underline{H})\cdot(\nabla\times\underline{H})\right] \tag{11}$$

The classical modeling of MHD assumes that there are no free electric charges in the fluid.[5,7] With these assumptions Maxwell's system for steady electro-magnetics of a moving media becomes

$$\nabla\cdot\underline{B} = 0 \tag{12}$$

$$\nabla\times\underline{H} = \underline{J} \tag{13}$$

$$\nabla\cdot\underline{J} = 0 \tag{14}$$

Ohm's law relates the induced electric current to the magnetic intensity vector in a moving media.

$$\underline{J} = \sigma\underline{v}\times\underline{B} \tag{15}$$

If electric conductivity and magnetic permeability are assumed to be constant within each phase, then the following non-dimensionalized magnetic field transport equation for the phase-changing MHD flow can be obtained from Eqs. (12) to (15). It needs to be solved intermittently[6] with Eqs. (8) through (11).

$$\frac{\partial\underline{H}}{\partial t} - \nabla\times(\underline{v}\times\underline{H}) = \frac{f/(\sigma_\ell\mu_\ell) + (1-f)/(\sigma_s\mu_s)}{P_mR_e}\nabla^2\underline{H} \tag{16}$$

The modified magnetic transport equations (16), the continuity equation (8), the modified linear momentum balance equations (9), and the modified energy balance equation (11) were integrated numerically using a finite volume method for structured clustered grids written in terms of non-orthogonal boundary-conforming coordinates.[9] Artificial density formulation was used to remove the singularity from the Navier-Stokes system, and the artificial time integration was performed using a four-stage Runge-Kutta algorithm.

EXAMPLES OF COMPUTED MHD FLOWS WITH SOLIDIFICATION

First, let us consider the problem of steady state solidification in two square-shaped containers without any magnetic field. Each container had the following

Table 1. Physical properties of molten and solid silicon.[9]

$\rho_\ell = 2550\,\text{kg/m}^3$	$\rho_s = 2330\,\text{kg/m}^3$
$c_p\ell = 1059\,\text{J/kg K}$	$c_{ps} = 1038\,\text{J/kg K}$
$\kappa_\ell = 64\,\text{W/m K}$	$\kappa_s = 22\,\text{W/m K}$
$T_\ell = 1685\,\text{K}$	$T_s = 1681\,\text{K}$
$\sigma_\ell = 12.3 \times 10^5\,1/\Omega\,\text{m}$	$\sigma_s = 4.3 \times 10^4\,1/\Omega\,\text{m}$
$\mu_{v\ell} = 7.018 \times 10^{-4}\,\text{kg/m s}$	$\mu = 7.022 \times 10^{-4}\,\text{kg m/A}^2\,\text{s}^2$
$L = 1.803 \times 10^6\,\text{J/kg}$	$\alpha = 1.4 \times 10^{-4}\,1/\text{K}$

Table 2. Parameters for two test cases.

Case 1 (small container)	Case 2 (large container)
$l_r = 0.01\,\text{m}$	$l_r = 0.02\,\text{m}$
$\text{Re} = 1000$	$\text{Re} = 1000$
$B_r = 0.1\,\text{T}$	$B_r = 0.1\,\text{T}$
$v_r = 2.7522 \times 10^{-2}\,\text{m/s}$	$v_r = 1.3761 \times 10^{-2}\,\text{m/s}$
$\text{Pr} = 1.1613 \times 10^{-2}$	$\text{Pr} = 1.1613 \times 10^{-2}$
$\text{Gr} = 1.8132 \times 10^5$	$\text{Gr} = 1.4506 \times 10^6$
$\text{Ra} = 2.1056 \times 10^3$	$\text{Ra} = 1.6845 \times 10^4$
$\text{Fr} = 8.7870 \times 10^{-2}$	$\text{Fr} = 3.1067 \times 10^{-2}$
$\text{Ec} = 7.1524 \times 10^{-8}$	$\text{Ec} = 1.7881 \times 10^{-8}$
$\text{Ht} = 4.1864 \times 10^1$	$\text{Ht} = 8.3729 \times 10^1$

thermal boundary conditions: left wall at T_c, right wall at T_h, and top and bottom walls thermally insulated. Gravity was assumed to act vertically downwards. Physical properties of molten and solid silicon (Table 1) were used in these two example test cases. T1

The physical properties of the liquid phase from Table 1 were adopted as the reference properties. For $\Delta T_r = T_h - T_c = 10\,\text{K}$, and $\text{Re} = 1000$, the resulting non-dimensional parameters are given in Table 2 for two different sizes of solidification containers, it should be noted out that these test cases used the physical properties for silicon with one exception. The magnetic Prandtl number that was used was three orders of magnitude larger than its physical value. This was done because the realistic extremely small values of P_m caused the explicit numerical integration algorithm used in the MHD analysis to diverge. T2

Figures 1 and 2 present the results for both test cases without magnetic field applied ($\text{Ht} = 0.0$) using two different grid sizes. F1 F2

In both test cases, the results for the coarser grid (50×50 grid cells) are very similar to the results with a refined grid (80×80 grid cells). The coarser grid was used for the MHD solidification simulations during the optimization process. Figure 3 shows the convergence history for containers of both sizes when using a grid size of 50×50 grid cells. F3

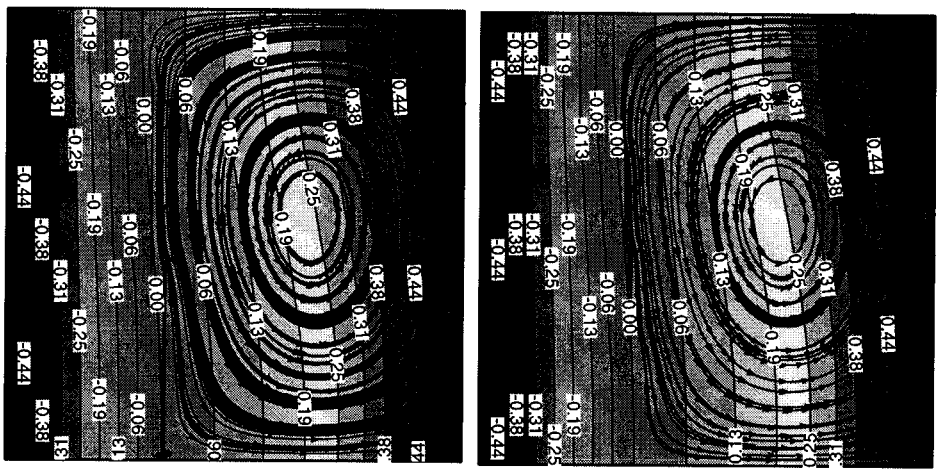

(a) 50 x 50 grid cells (b) 80 x 80 grid cells

Figure 1. Temperature field and streamlines for smaller container using two grid sizes (Ht = 0.0).

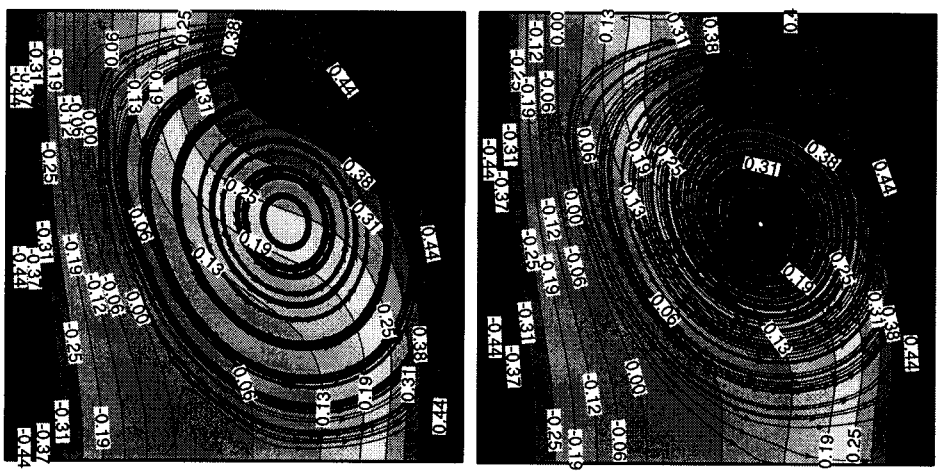

(a) 50 x 50 grid cells (b) 80 x 80 grid cells

Figure 2. Temperature field and streamlines for larger container using two grid sizes (Ht = 0.0).

OPTIMIZATION OBJECTIVES AND ALGORITHMS

A variety of optimization algorithms have been developed and used for problems from many different disciplines. Various optimization algorithms have

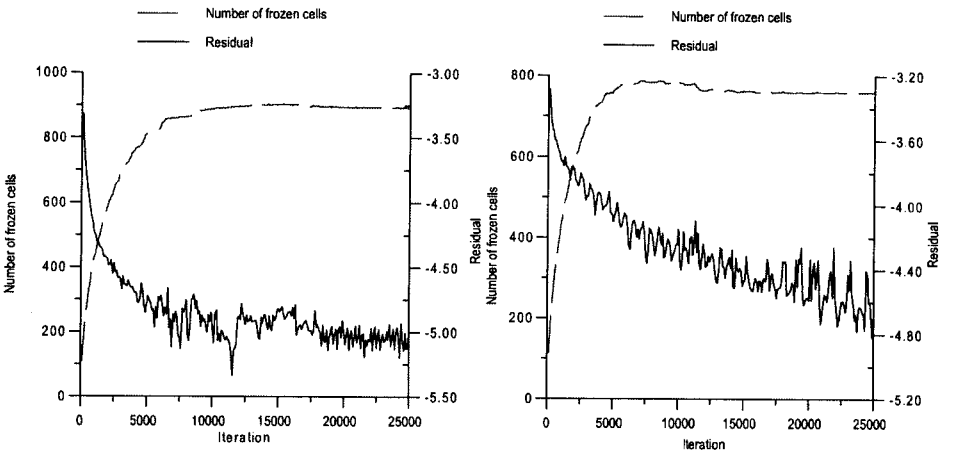

(a) Smaller container (b) Larger container

Figure 3. Convergence history for solidification in both containers (Ht = 0; grid 50 × 50 cells).

been known to provide different rates of convergence depending on the size and shape of the mathematical design space, the nature of the constraints, and where they are during the optimization process. This is why we created a hybrid constrained optimization computer program[10] that incorporates several of the most popular optimization modules: the Davidon-Fletcher-Powell (DFP) gradient search method, a genetic algorithm (GA), the Nelder-Mead (NM) simplex method, quasi-Newton algorithm of Pshenichny-Danilin (LM), differential evolution (DE), and sequential quadratic programming (SQP). The original package did not have the DE, SQP, and LM methods. A set of analytic rules were coded into the program to automatically switch among the different optimization algorithms to avoid local minima and to accelerate the overall convergence. Different versions of this hybrid optimization package have been successfully applied during the optimization of various multi-disciplinary problems.[11] Another conceptually different optimizer, known as IOSO, was also used in this work. It is based on semi-stochastic methods and self-adaptive response surface methodology.[11,12] Different numerical analysis methods (finite volume and finite element methods) and different optimization algorithms (a hybrid optimizer and a IOSO optimizer) were used to demonstrate and compare their respective accuracies, robustness, and versatility.

MINIMIZATION OF THE NATURAL CONVECTION USING MHD AND A HYBRID OPTIMIZER

It is well known that application of a magnetic field to a solidifying flow-field of an electrically conducting fluid will create additional body forces that are

capable of significantly altering the flow-field and heat transfer.[13–16] It has also been demonstrated that it is possible to optimize the boundary values of the magnetic field with the objective of achieving certain desired features of the flow-field.[17,18] Let us now try to optimize the magnetic field applied on each of the four walls of the square container of test case 1 (smaller container) described in the previous section. The objective is to minimize the effects of the thermally induced natural convection in case of solidification from a sidewall. To satisfy magnetic flux conservation (Eq. 12), we consider the simple case of periodic boundary conditions.

$$B_1(0, y) = B_2(1, y) \tag{17}$$

$$B_3(x, 0) = B_4(x, 1) \tag{18}$$

The unknown boundary values of the magnetic field were parameterized as follows:

$$B(x_k) = \sum_{i=1}^{M} P_i C_i(x_k) \tag{19}$$

where P_i is unknown parameter and the function $C_i\,(x_k)$ is given as AQ3

$$C_i(x_k) = \cos\left[(i-1)\frac{\pi}{2}x_k\right] \quad \text{for } i = 1, 3, 5, \ldots \tag{20}$$

$$C_i(x_k) = \cos\left[i\frac{\pi}{2}x_k\right] \quad \text{for } i = 2, 4, 6, \ldots \tag{21}$$

The objective function for this optimization problem was to minimize the sum of all vertical temperature gradient magnitudes in the entire liquid region that should minimize thermally induced buoyancy flow-field in the melt. Thus, our problem is to minimize the objective function, F, defined as

$$F = \left[\frac{1}{\#\text{liquid cells}} \sum_{i=1}^{\#\text{liquid cells}} \left(\frac{\partial T}{\partial y}\right)^2\right]^{1/2} \tag{22}$$

In all test cases, the initial guess for the parameters was zero, while the number of optimization population members was equal to three times the number of parameters. The hybrid optimizer started with the DE method in all test cases and the initial population was randomly generated around the initial guess.

Figures 4a and b show the results for the test case 1 without an applied magnetic field and with an optimized magnetic field applied. One can see that the buoyancy effects are reduced. In this test case, three parameters were used for $B_1(0, y)$ and three parameters were used for $B_3(x, 0)$. Figure 5 shows the optimized boundary conditions, where one can see that the magnetic field is constant at the boundaries $y = 0.0$ and $y = 1.0$. F4 F5

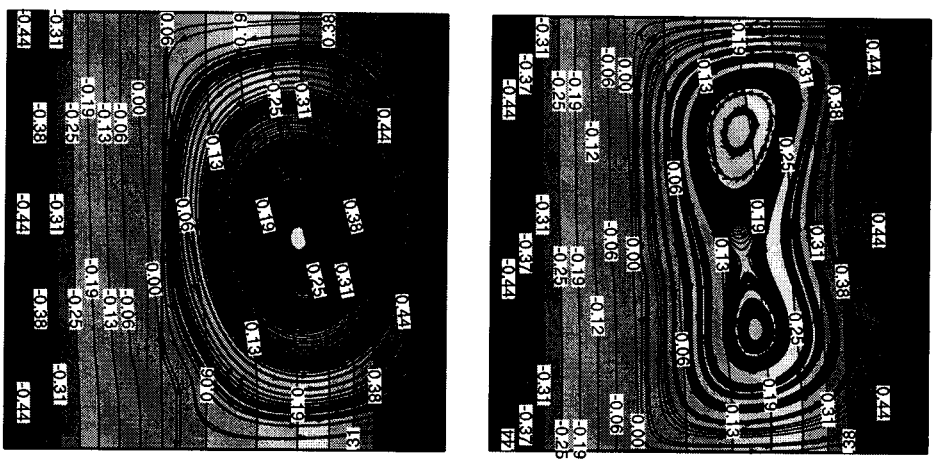

a) b)

Figure 4. Isotherms and streamlines without: (a) and with (b) an optimized applied magnetic field (test case 1: smaller container).

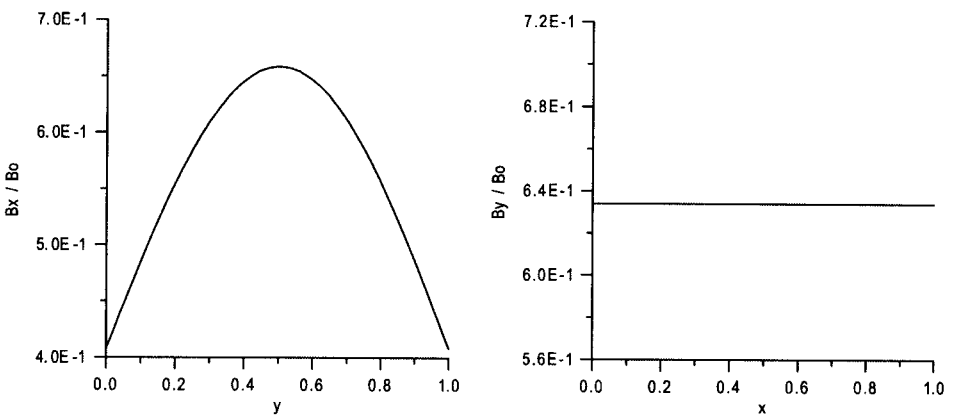

Figure 5. Optimized magnetic field boundary conditions (test case 1: smaller container).

Figure 6 shows the convergence history for the hybrid optimizer in this case where the DE and NM optimization modules were automatically used most often. F6

Figure 7 shows the results for test case 2 (a larger container) without an applied magnetic field and with an optimized magnetic field applied. One can see that the buoyancy effects are reduced, but not eliminated. Again, three parameters were used for $B_1(0, y)$ and three parameters for $B_3(x, 0)$, while periodic boundary conditions were enforced on the opposite boundaries. Figure 8 shows the optimized boundary conditions, where, again, the variation of the magnetic field along the boundaries $x = 0.0$ and $x = 1.0$ is greater than at the boundaries $y = 0.0$ and $y = 1.0$. F7 F8

200031887_LMMP19_04_R1_081204

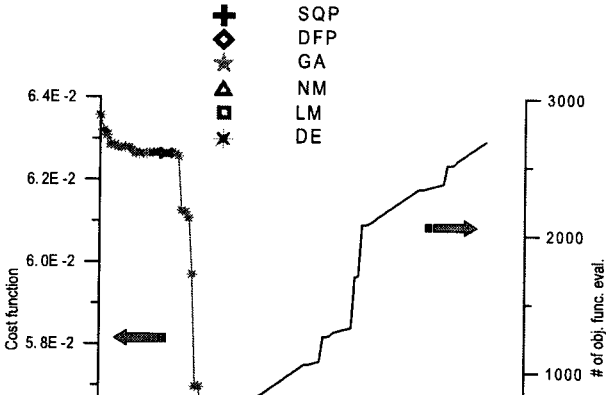

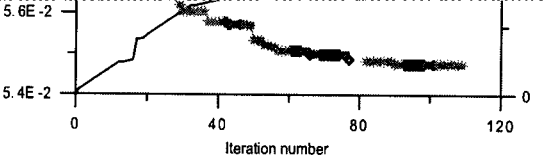

Figure 6. Convergence history for the hybrid optimizer (test case 1: smaller container).

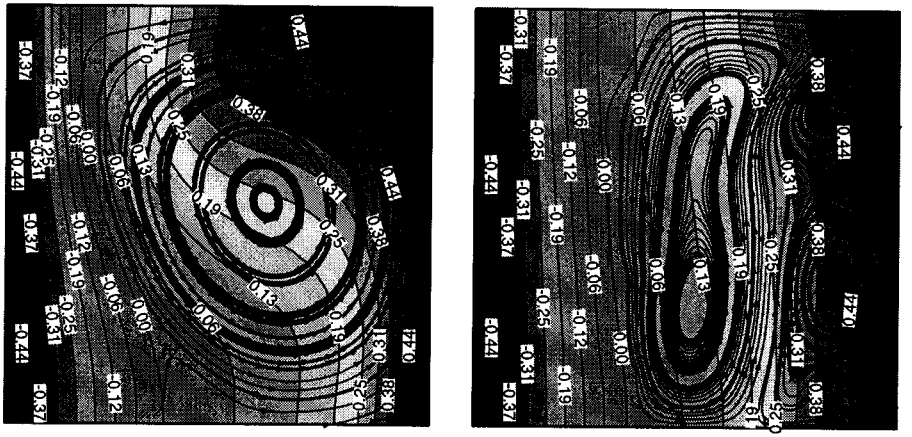

a) b)

Figure 7. Isotherms and streamlines without: (a) and with (b) an optimized applied magnetic field (test case 2: larger container).

Figure 9 shows the convergence history for the hybrid optimizer in this test case where only the DE, GA, and NM optimization modules were automatically applied. **F9**

Figures 10 through 12 show the results for test case 2, but using six parameters for $B_1(0, y)$ and six parameters for $B_3(x, 0)$, instead of the three parameters used **F10–F12**

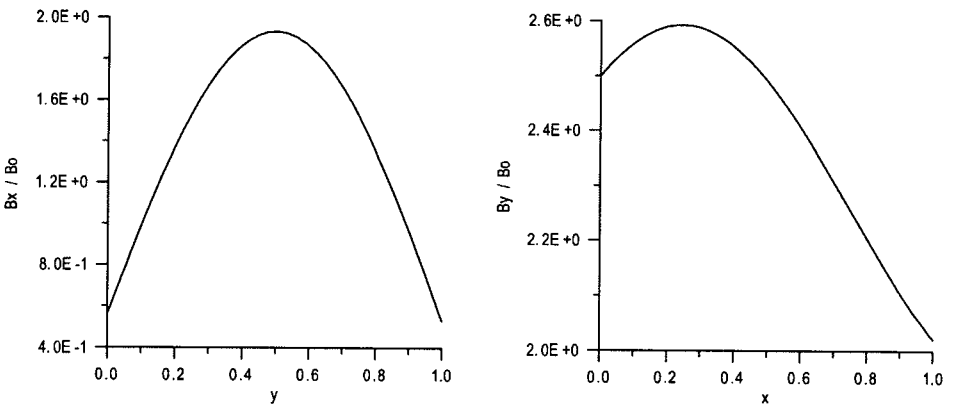

Figure 8. Optimized magnetic field boundary conditions (test case 2: larger container).

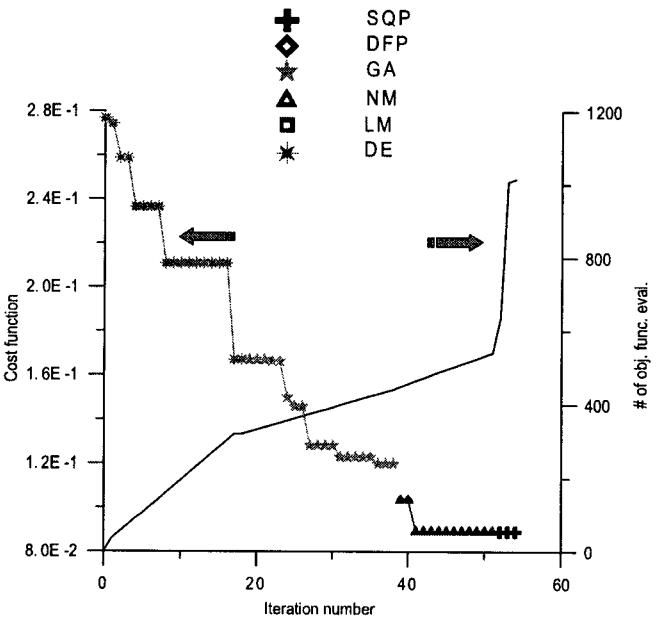

Figure 9. Convergence history for the hybrid optimizer (test case 2: larger container).

before. One can see that the natural convection effects are further reduced in this case. It is interesting to note that the variation of the applied magnetic field is greater at the boundaries $y = 0.0$ and $y = 1.0$.

Figure 12 shows the convergence history, where, again, we applied the DE and GA modules. In fact, the GA module did the entire job in this test case.

+ [12.8.2004–7:54pm] [1–24] [Page No. 12]
K:/Journals/Inpro/MDI/LMMP/LMMP19(4)/200031887.3d Materials and Manufacturing Processes (LMMP)

200031887_LMMP19_04_R1_081204

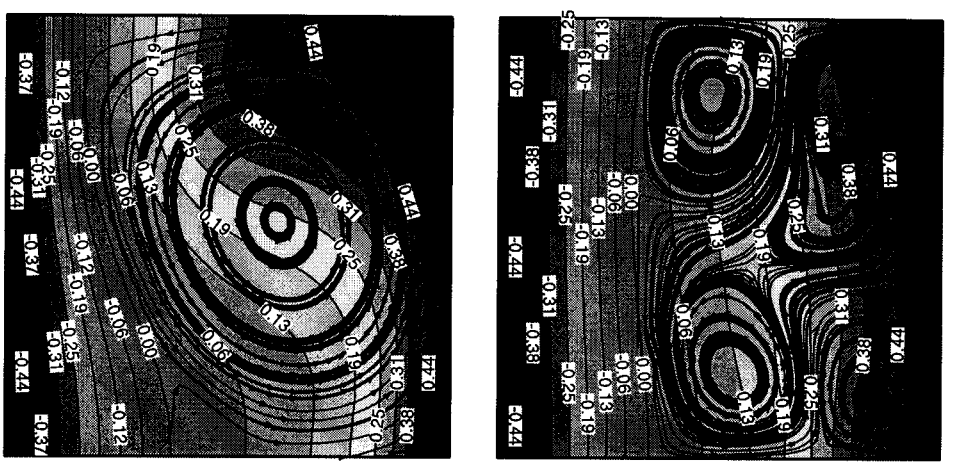

Figure 10. Isotherms and streamlines without and with an optimized applied magnetic field (test case 2 with six parameters).

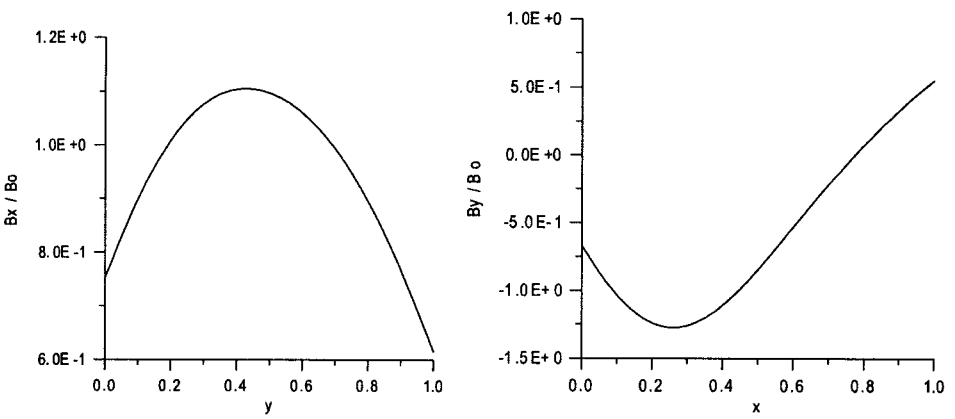

Figure 11. Optimized magnetic field boundary conditions (test case 2 with six parameters).

MHD SOLIDIFICATION OPTIMIZATION USING LSFEM AND IOSO OPTIMIZER

Other possibly more robust and accurate numerical integration methods were explored[14,15] to allow for physical values of the magnetic Prandtl number and for significantly higher values of viscosity in the solid region. Consequently, we will present a combination of MHD with solidification where the numerical analysis was performed with a least squares spectral finite element method (LSFEM),[15,18] and

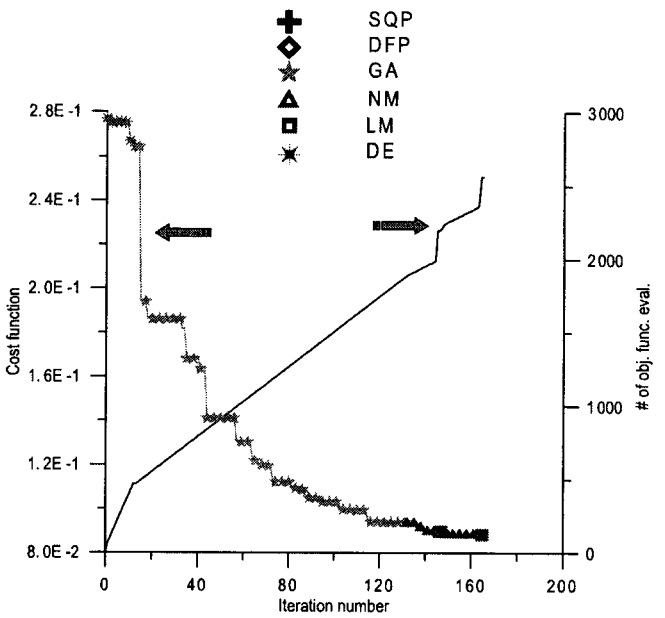

Figure 12. Convergence history for the hybrid optimizer (test case 2 with six sensors).

the optimization was performed using a self-adaptive response surface-based semi-stochastic algorithm[11,12] called IOSO. Here, the objective of the optimization is to minimize the velocity magnitude of the melt flow near the solid-liquid interface. The optimizer searches for this by changing the orientation and distribution of the sidewall magnets as well as the strength of the applied external uniform vertical magnetic field. The objective function was expressed as the following equation:

$$F = \sum_{i=1}^{N_{\text{fluid}}} \sqrt{u_i^2 + v_i^2} \tag{23}$$

Here, N_{fluid} is the total number of grid points located between $y > 0.04$ m and $y < 0.08$ m—that is, only in the flow-field region adjacent to the solid/melt interface. The only constraints considered in this problem were the bounds on the magnitudes of the design variables. In this problem, we considered a container with relatively weak magnets embedded in the sidewalls. The magnetic flux density strength and distribution was parameterized using a B-spline with control variables located at 7 points along the wall ($y = 0.0$, 0.02, 0.04, 0.06, 0.08, 0.1 m). These design variables controlled the magnitude, direction, and distribution of the magnetic field.

Two cases were run. For case 1, each control point was allowed to vary from 0.07 Tesla to −0.07 Tesla. In case 2, each control point was allowed to vary from 0.5 Tesla to −0.5 Tesla. This distribution was applied to the right wall. The distribution on the left wall was taken to be of equal magnitude, but opposite sign to that of the right wall. Therefore, the resulting magnetic field was always symmetrical with

+ [12.8.2004–7:54pm] [1–24] [Page No. 14]
K:/Journals/Inpro/MDI/LMMP/LMMP19(4)/200031887.3d Materials and Manufacturing Processes (LMMP)

200031887_LMMP19_04_R1_081204

respect to the y-axis. A vertical magnetic field was also applied so that it could be generated using an electromagnet located on the top and bottom of the container. The optimized magnetic potential produced a uniform vertical field strength varying between 0.0 Tesla to 0.15 Tesla in case 1 and between 0.0 Tesla and 0.5 Tesla in case 2. For this example, the total number of design variables was seven.

The optimization procedure was applied to the solidification of a silicon melt in a square container with sides of 0.1 m. A uniform temperature of 1676.0 K was applied to the top wall so that solidification occurred on the top wall of the container. A parabolic temperature profile was applied to the hot bottom of the container to simulate nonuniform heating of the melt. The temperature at the center of the bottom wall was 1688.0 K, and the temperature at the bottom corners was set to 1686.0 K. The sidewalls were thermally insulated. A no-slip condition for velocity was enforced on all walls of the container. The magnetic flux density determined from the B-spline parameterization was specified directly on the sidewalls. A constant magnetic potential was specified on the top and bottom of the container. The potentials were determined by calculating the potential required to produce a uniform vertical field of a specified strength. A relatively coarse quadrilateral computational grid with $17 \times 17 = 289$ elements with a p-level of $P = 3$ was used with the LSFEM code (Fig. 13). F13

The p-version of LSFEM was used to compute all results reported here. The order of the approximation function was increased, or enriched, until the desired level of convergence was obtained. In this case, the size of the grid was fixed and the order of the approximation was increased uniformly across the grid. For problems with smooth solutions, the p-version of the LSFEM converged to the exact solution at an exponential rate as the number of unknowns was increased by the uniform enrichment of the element approximation functions.

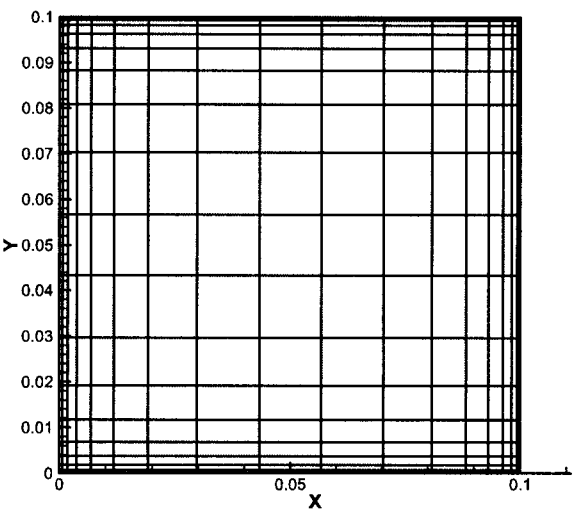

Figure 13. Computational grid for FEM analysis.

In cases where the mushy region was only one grid cell wide, the effective heat capacity including the latent heat release was computed using an enthalpy method.[15,19]

$$\rho C^{eq} = \frac{dH}{dT} \approx \frac{|\nabla H|}{|\nabla T|} \tag{24}$$

Using this treatment in the mush region allowed much larger values of the viscosity to be specified in the solid phase. Specifically, LSFEM/MHD solidification with the enthalpy method used seven orders of magnitude higher viscosity in the solid phase than in the liquid phase. Figures 14 and 15 show velocity field and streamlines **F14 F15**

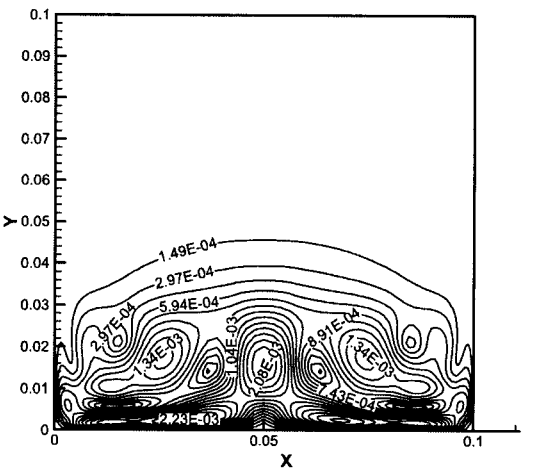

Figure 14. Velocity magnitudes with no applied magnetic field—FEM analysis.

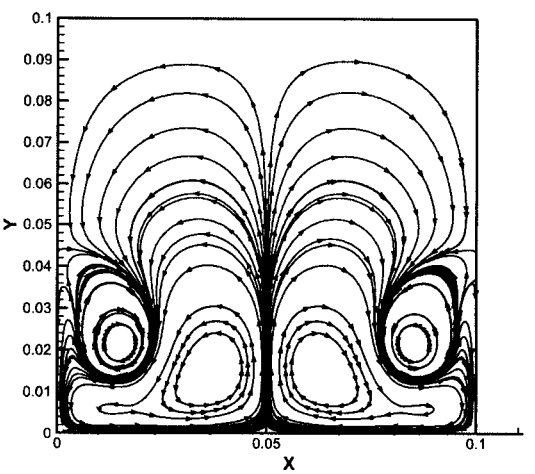

Figure 15. Streamlines with no applied magnetic field—FEM analysis.

[12.8.2004–7:54pm] [1–24] [Page No. 16]
K:/Journals/Inpro/MDI/LMMP/LMMP19(4)/200031887.3d Materials and Manufacturing Processes (LMMP)

200031887_LMMP19_04_R1_081204

computed without the application of a magnetic field. Correct physical value of the magnetic Prandtl number was used in all simulations based on LSFEM/MHD.

The IOSO algorithm was used to optimize the applied magnetic field to this problem.[12,11] The optimization code was executed on a commodity component-based parallel computer with Pentium II processors (400 MHz speed). Twenty processors were used, and the total execution time was about 16 h. The initial guess given to the optimizer was that all design variables were set to zero. In other words, the initial guess was a flow-field without any applied magnetic field. In that case the normalized value of the objective function is 1.0. AQ5

LSFEM: Case 1

In this case, the sidewall magnetic field strengths were very weak. They varied between 0.07 T and 0.07 T. A maximum strength for uniform vertical field varied between 0.0 T and 0.15 T. After 12 iterations, the IOSO-based optimizer achieved its best objective function value of 0.292. In comparison, the objective function for a simple case of no sidewall magnets and a maximum strength uniform vertical field of 0.15 T achieved a value of 0.771. The optimized magnetic field reduced the average velocity in the melt region between $y = 0.04$ m and $y = 0.08$ m by more than a factor of three. Figures 16 and 17 demonstrate that the magnetic field effectively damped the flow field circulation, removing the pair of secondary vortices present in the case with no applied magnetic field. Figure 18 shows the optimized magnetic field lines of flux density. F16 F17 F18

In the lower half of the sidewall, the magnets were at maximum strength of 0.07 T. Above that, the polarity changed and the strength of the sidewall magnet was reduced to 0.04 T at the top of the container (Fig. 19). For the top and bottom walls, F19

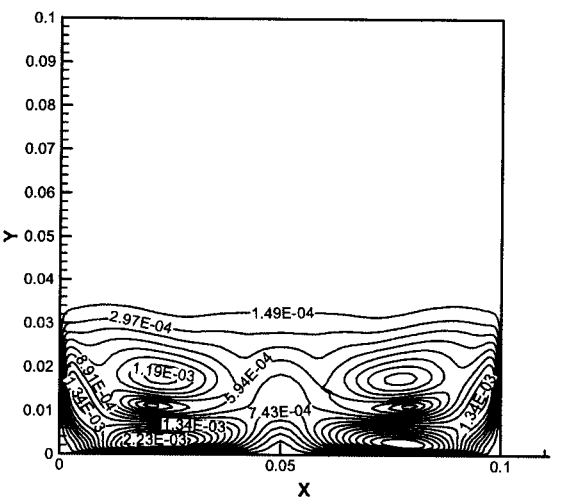

Figure 16. Velocity magnitudes with optimized applied magnetic field (case 1).

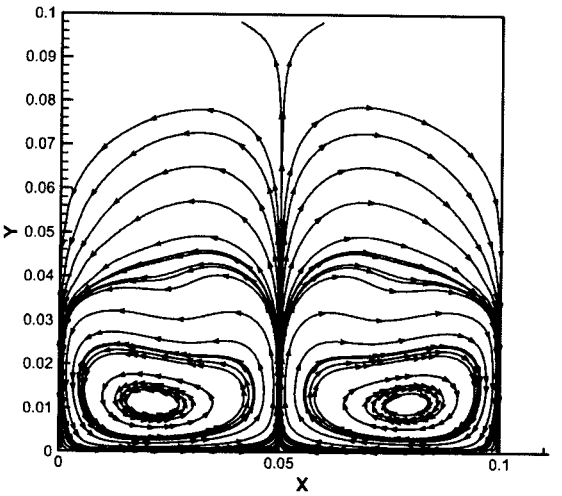

Figure 17. Streamlines with optimized applied magnetic field (case 1).

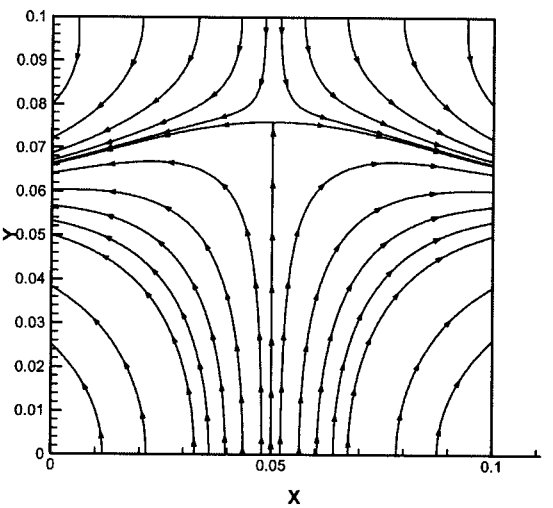

Figure 18. Lines of magnetic flux for the optimized applied magnetic field (case 1).

the optimizer chose a magnetic potential that would produce a uniform vertical field of 0.025 T. This is interesting since the optimizer had the choice of producing up to 0.15 T but yet converged to a much smaller value. This indicates that by damping the melt circulation, the shape of the magnetic field was as important as its strong vertical component. Figure 20 compares the temperature distribution between flow with no magnetic field and flow with optimized magnetic field. The optimized field clearly smoothes the temperature contours due to the reduced convection. F20